Ligand bridged MXene/metal organic frameworks heterojunction for efficient photocatalytic ammonia synthesis

Zhengfeng Shen [a], Feifei Li [a], Lijun Guo [a], Xiaochao Zhang [a], Yawen Wang [a], Yunfang Wang [a], Xuan Jian [b], Xiaoming Gao [b], Zhongde Wang [a], Rui Li [a,c,*], Caimei Fan [a], Jianxin Liu [a,**]

[a] *Key Laboratory of Coal Science and Technology Ministry of Education, College of Chemical Engineering and Technology, Taiyuan University of Technology, Taiyuan 030024, PR China*
[b] *College of Chemistry and Chemical Engineering, Shaanxi Key Laboratory of Chemical Reaction Engineering, Yan'an University, Yan'an 716000, PR China*
[c] *Shanxi Key Laboratory of Compound Air Pollutions Identification and Control, College of Environmental Science and Engineering, Taiyuan University of Technology, Taiyuan 030024, PR China*

ARTICLE INFO

ABSTRACT

Efficient interfacial charge transfer is imperative for enhancing N_2 photofixation, yet controlling this process proves challenging. Herein, a unique ligand pre-coupling strategy was employed to design ligand-bridged MXene/MIL-125(Ti), creating a coordination bond between $Ti_3C_2O_x$ and MIL-125(Ti) and forming a ligand-bridge, aiming to regulate interfacial electron transfer. Kelvin probe force microscopy and charge density difference analysis revealed the establishment of an electronic unidirectional transport channel from MIL-125(Ti) to $Ti_3C_2O_x$ through this ligand-bridge. This effectively reduced the interface charge transfer resistance, enhanced the separation efficiency of charge carriers. Consequently, the $Ti_3C_2O_x$/MIL-125(Ti) manifested an excellent ammonia evolution rate of 103.02 $\mu mol \cdot g_{cat}^{-1} \cdot h^{-1}$. Furthermore, the efficiency of this strategy for accelerating the separation of photogenerated carriers was demonstrated in five other MOFs, demonstrating its potential for constructing ligand-bridged MXene/MOFs heterojunctions.

1. Introduction

The reduction of dinitrogen into ammonia plays a critical role in the global loop of N elements and is indispensable to life agriculture and industrial processes on earth [1]. However, the industrial Haber-Bosch process often faces harsh reaction conditions and significant energy consumption, resulting in numerous environmental and energy-related challenges [2,3]. Currently, the fascinating and carbon-free photocatalytic technology for ammonia synthesis under ambient conditions has attracted increasing attention in the field [4–7]. To date, diversiform photocatalysts such as TiO_2, WO_3, BiOX, CdS, g-C_3N_4, LDH, LaOF el at. have been investigated for photocatalytic ammonia synthesis [8–15]. Considering the predictable and customizable three-dimensional micro mesoporous network structure, the abundant specific surface area and adsorption sites, Metal-organic frameworks (MOFs) have attracted much attention in photocatalytic ammonia production [16–18]. Among them, The titanium-based MOFs with low toxicity, suitable photoredox

properties, and high stability are regarded as potential photocatalysts capable of ammonia synthesis [19–24]. Nevertheless, the challenge of severe recombination of photogenerated carriers still remains to be resolved.

Despite it is the consensus that incorporating co-catalysts into MOFs is an efficient means to enhance electron-hole pair separation, challenges persist in facilitating the interaction between MOFs and co-catalysts to enable efficient charge transfer [25–29]. The heterogeneous interfaces coordination engineering strategy provides a viable solution, chemically bonded interactions between component interfaces have been utilized to improve electron transfer during the photocatalytic reduction of small molecules (CO_2, N_2, H_2O), and degradation of organic matter on heterojunctions and atomically dispersed metal catalysts [30–34]. As reported by Liu's group, they designed a densely linked titanium porphyrin metal organic framework−$ZnIn_2S_4$ core−-shell heterojunction through −N − Zn− coordination bonds [35]. Similarly, Gregor's team achieved the coupling of benzoic acid to Au

(111) and observed remarkably fast charge transfer through phenyl [36]. These interfacial chemical bonds served as directed carrier transfer channels, enhancing charge separation efficiency. Therefore, constructing a chemical bond between the MOF and the co-catalyst interface can increase the overlap density of electrons and create a directional, shorter carrier transport channel at the interface, thus the performance of catalyst can be improved.

Currently, additional surface modifiers are commonly required to create docking sites that establish a connection between two materials, enabling them to surmount the high interfacial energy barrier and form a strong bond to enhance charge transfer [37–39]. Ma's group reported the successful construction of the UiO-66-NH$_2$ (Zr/Ti)/carboxyl-functionalized MXene composites through addition of phenyl-carboxylic acid diazonium salt for auxiliary coordination, which exhibited excellent hydrogen evolution reaction activity [40]. Our team also used ethylene glycol (EG) as a molecular bridge connecting palladium (Pd) and bismuth oxybromide (BiOBr) and accelerated carrier separation through the redistribution of the electron cloud between the components [41]. However, surfactants present a double-edged sword, as they can also detrimentally effect MOFs by diminishing the surface area and available reaction sites. Therefore, directly utilizing the organic ligands of MOFs as anchored bridges to form coordination bonds with co-catalysts is a comprehensive method. Unfortunately, MOFs−cocatalysts heterojunctions bridged by the organic ligands of MOFs have rarely been observed, and the associated adjustments in the local structure, charge transfer mechanism, and photocatalytic performance remain unknown.

Herein, the most representative Ti$_3$C$_2$T$_x$ MXene, with abundant active terminal groups that enable it to coordinate with organic ligand functional groups, was selected as a co-catalyst [42–44]. A novel ligand pre-coupling strategy (Scheme 1) was employed to synthesize ligand bridged MXene/MIL-125(Ti) complexes (Ti$_3$C$_2$O$_x$/MIL-125(Ti)), maintaining the surface area of MOFs and creating tightly coupled MOF-based heterojunctions with high carrier separation ability. Modern spectroscopy and quantum computing were utilized to analyze the ligand-bridge effect, which revealed the coordination mechanism between Ti$_3$C$_2$O$_x$ and BDC (Terephthalic acid (H$_2$BDC)) is the lone pair of electrons from C=O in Ti$_3$C$_2$O$_x$ into the empty orbitals of the hydroxyl oxygens in BDC to form a coordination bond. These coordination connections not only overcome the interfacial energy barrier between the two materials but also establish an electronic unidirectional transport channel from MIL-125(Ti) to Ti$_3$C$_2$O$_x$. Consequently, Ti$_3$C$_2$O$_x$/MIL-125 (Ti) can continuously hydrogenate nitrogen molecules via an alternative pathway to synthesize ammonia under simulated sunlight irradiation, achieving 3.25, and 2.51 times the activity of the pure MIL-125(Ti) and Ti$_3$C$_2$O$_x$+MIL-125(Ti) composites. Furthermore, the ligand pre-coupling strategy demonstrates a universality capability in improving the separation of photogenerated carriers for five other MOFs (MOF-5, UIO-66 (Zr), UIO-66(Ce), MIL-101(Fe), Cu-BDC).
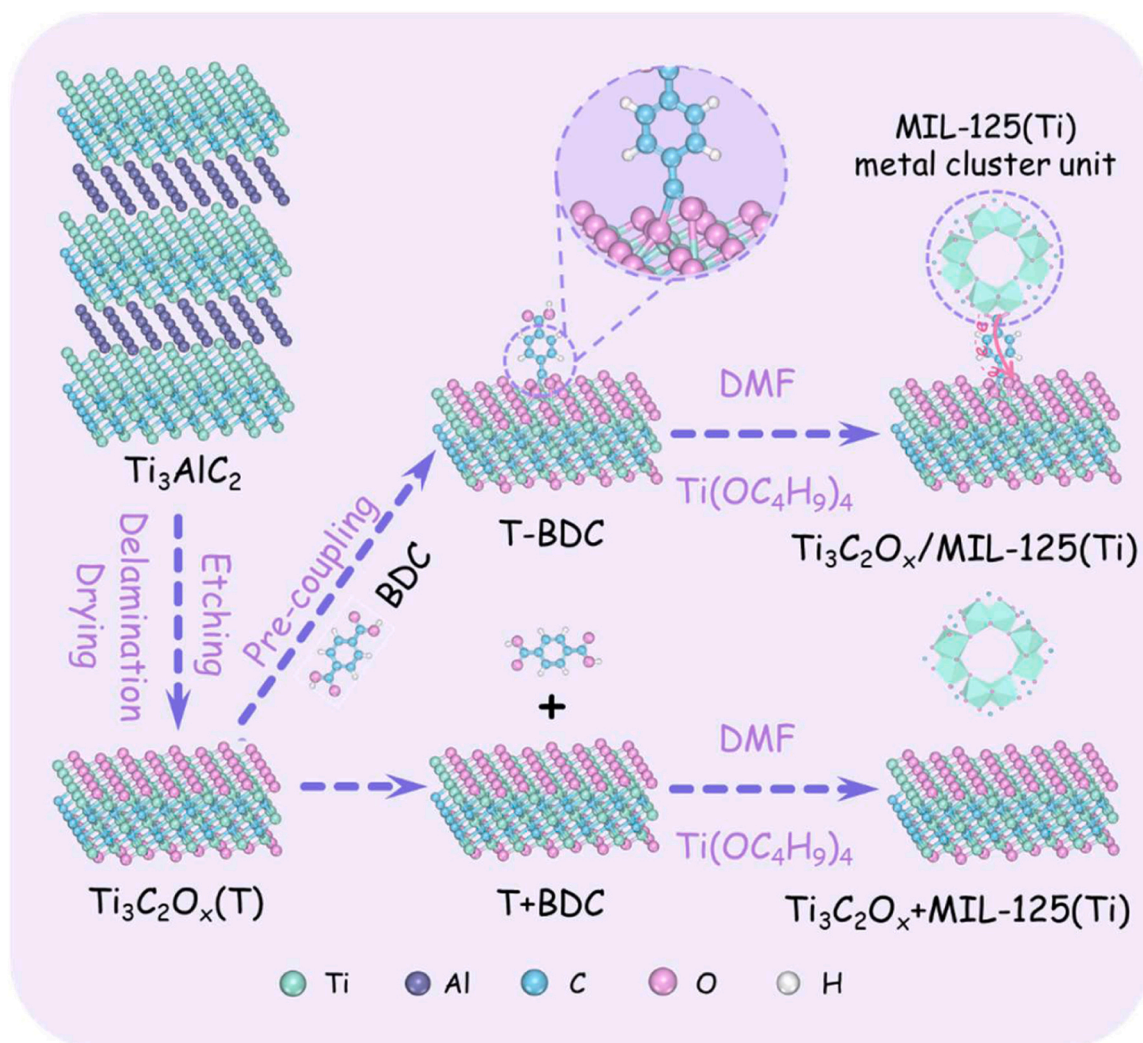
Scheme 1. Schematic illustration of photocatalyst preparation with/without pre-coupling ligands.

2. Experimental

2.1. Preparation of $Ti_3C_2O_x$ (T) and the ligand pre-coupling with $Ti_3C_2O_x$ (T-BDC)

The $Ti_3C_2O_x$ MXene was synthesized by in-situ HF etching and ultrasound-assisted delamination of MAX (Ti_3AlC_2). Briefly, the MAX was immersed in an in-situ HF solution (containing 1 g LiF and 20 ml 9 M HCl) and stirred 24 h at 35 °C. Then, the above-gained etched product was centrifuged (3500 rpm) and washed with deionized water until the pH> 6 of the supernatant. Finally, the above-collected precipitate was added to 100 ml of deionized water, delaminated ultrasonically for 1 h under Ar atmosphere, centrifuged to obtain thin MXene solution, and freeze-dried to obtain fluffy $Ti_3C_2O_x$ solid. The ligand pre-coupling with $Ti_3C_2O_x$ was obtained by a simple co-grinding process between H_2BDC and $Ti_3C_2O_x$ solid with active terminal groups, denoted as T-BDC.

2.2. Preparation of MIL-125(Ti) and $Ti_3C_2O_x$/MIL-125(Ti) photocatalysts

The MIL-125(Ti) photocatalyst was synthesized according to a pre-existing literature procedure [21]. Simply, Terephthalic acid (H_2BDC) (1 g, 6 mmol) and tetra-n-butyl titanate ($Ti(OC_4H_9)_4$) (0.52 ml, 1.5 mmol) were added into a solution containing DMF (18 ml) and MeOH (2 ml). The above mixture was stirred at room temperature for 30 min and transferred to a 50 ml Teflon liner before being heated at 150 °C for 20 h. After reaction, the resultant suspension was centrifuged (3500 rpm) and washed with DMF and ethanol respectively, and dried to obtain the white solid product.

The x% $Ti_3C_2O_x$/MIL-125(Ti) was obtained by a similar process with some slight changes, only replaced H_2BDC with T-BDC ($Ti_3C_2O_x$ is 0.03, 0.075, 0.15, 0.225 mmol in 6 mmol H_2BDC, respectively) under the condition that the content of BDC and tetra-n-butyl titanate remained unchanged, denoted as x% $Ti_3C_2O_x$/MIL-125(Ti) (x represents the molar ratio of $Ti_3C_2O_x$ to n-butyl titanate, which is 2, 5, 10, 15, respectively). In addition, we also provided a detailed ingredient list for the preparation of x% $Ti_3C_2O_x$/MIL-125(Ti) in Table S1. For comparison, we also directly add the same content of $Ti_3C_2O_x$ into the reaction solution
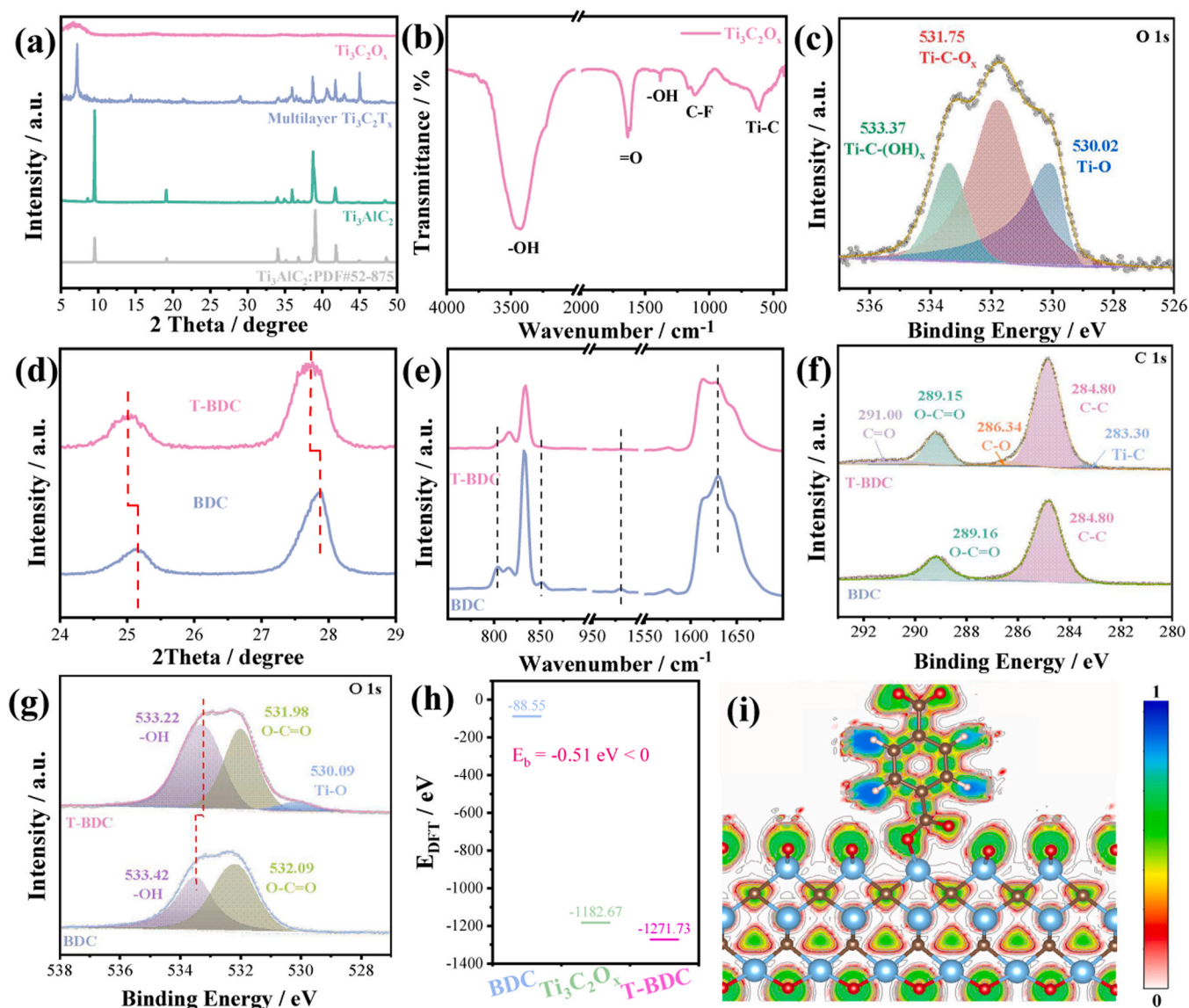
Fig. 1. (a) XRD patterns (b) FT-IR patterns and (c) O 1 s high-resolution XPS spectra of $Ti_3C_2O_x$; (d) XRD patterns (e) Raman patterns and (f, g) C 1 s and O 1 s high-resolution XPS spectra of BDC and T-BDC; (h) the ground state energy and (i) ELF slice map for T-BDC.

without co-grinding process to gain a series of photocatalysts, denoted as x% $Ti_3C_2O_x$+MIL-125(Ti) (x = 2, 5, 10, 15, respectively) (Scheme1).

3. Results and discussion

3.1. Characterization of $Ti_3C_2O_x$ (T) and T-BDC

The $Ti_3C_2O_x$/MIL-125(Ti) composites were prepared using novel and unique ligand pre-coupling strategies. As depicted in Scheme 1, $Ti_3C_2O_x$, as a pre-coupling agent, was first synthesized by in-situ HF etching, ultrasound-assisted delamination and drying process. Subsequently, $Ti_3C_2O_x$ is pre-coupled with the ligand BDC to yield T-BDC through a simple co-grind process, in which the carboxyl group of BDC coordinates to the surface oxygen active group of $Ti_3C_2O_x$, serving as a bridge to establish robust interactions between MIL-125(Ti) and $Ti_3C_2O_x$. Finally, the $Ti_3C_2O_x$/MIL-125(Ti) heterojunction composites are synthesized directly via a one-step solvothermal process using the pre-coupled ligand T-BDC and titanium tetrabutoxide.

The crystal morphology and surface chemical states of the pre-coupling agent ($Ti_3C_2O_x$) were characterized using X-ray diffraction (XRD), Fourier transform infrared spectroscopy (FT-IR), Raman spectroscopy, and X-ray photoelectron spectroscopy spectrum (XPS) (Fig. 1 and Figs. S1-S2). Fig. 1a illustrates XRD patterns exhibiting a noticeable blue shift (9.52→6.66) in the (002) diffraction peak of $Ti_3C_2O_x$ after etching, indicating the transition from the bulk phase to the thin layer of MXene and confirming the successful etching delamination [45]. Fig. 1b presents the FTIR patterns, revealing that the peaks at 3441 cm^{-1} and 1381 cm^{-1} represent the stretching vibration and the bending vibration of O-H (originating from the adsorbed H_2O or terminal -OH group on the $Ti_3C_2O_x$ surface), respectively. Observations of a distinct C=O bending vibrational peak at 1635 cm^{-1} and a weak C-F stretching vibrational peak at 1111 cm^{-1} indicate that the terminal groups on the surface of $Ti_3C_2O_x$ primarily consist of oxygen species. Furthermore, the Raman spectrum (Fig. S1) demonstrates that the surface of $Ti_3C_2O_x$ is predominantly composed of =O rather than -OH [46]. Additionally, the XPS high-resolution spectrums of O 1 s and Ti 2p (Fig. 1c and Fig. S2), as well as the statistical table of element content (Table S2), further confirm the dominant presence of terminal oxygen groups on the $Ti_3C_2O_x$ surface. These finding provides further confirmation of the abundant presence of terminal oxygen groups on the surface of $Ti_3C_2O_x$, establishing a solid basis for pre-coupling with BDC.

To demonstrate ligand bridged $Ti_3C_2O_x$/MIL-125(Ti) heterojunctions were established, the successful pre-coupling $Ti_3C_2O_x$ with the ligand BDC should be proved firstly. XRD was carried out to investigate the changes in the crystalline structure of the ligand BDC before and after pre-coupling with $Ti_3C_2O_x$. The diffraction patterns of T-BDC and BDC standard product closely resemble each other, but no characteristic diffraction peaks of $Ti_3C_2O_x$ are observed, which may be due to its weak strength, low content and high dispersion [47] (Fig. S3). Interestingly, the diffraction peaks at 25° and 28° both exhibit a blue shift of the same magnitude in the T-BDC (Fig. 1d), which is attributed to the local lattice distortion of BDC induced by the strong coordination of C=O of $Ti_3C_2O_x$ with -COOH of BDC resulting in the increase of its crystal spacing (further support for this claim is provided by additional XPS analysis and DFT calculations). To provide further confirmation of the pre-coupling, the molecular structure and chemical state of the ligand BDC with/-without pre-coupled $Ti_3C_2O_x$ were explored using FT-IR, Raman and XPS spectroscopy. As expected, the FT-IR spectra of BDC and T-BDC exhibit identical absorption peaks for hydroxy and carboxyl groups (Fig. S4), and the Raman patterns present similar characteristic peaks (Fig. 1e and Fig. S5). Based on existing literature [48–50] and the Raman standard spectrum of BDC in the AIST database (SDBS No.: 673), the Raman peaks at 1629, 1576, 1450, 1408, 1320, 1288, 1181, 1124, 981, 851, 832, 815, 804, 672, 634 cm^{-1} (Fig. S5) are identified as characteristic of BDC. More precisely, the peaks at 1629, 1450, 111, and 1124 cm^{-1} correspond to in-plane vibration modes of the aromatic ring,

while the peaks at 851 and 634 cm^{-1} correspond to C-H stretching or out-of-plane vibration modes of the aromatic ring on the benzene ring, and the other characteristic peaks are related to the carboxyl vibration on the benzene ring. Surprisingly, Fig. 1e illustrates that the characteristic peaks at 981, 851, 804, and 1629 cm^{-1} in T-BDC disappear or weaken after pre-coupling with $Ti_3C_2O_x$ (indicated by the dashed line in Fig. 1e), confirming the coupling site located on the carboxyl group of BDC. In contrast, there were no significant differences observed in the IR and Raman characterization before and after direct physical mixing $Ti_3C_2O_x$ and BDC in DMF solvent (without pre-coupling and denoted as T+BDC) (Figs. S6-S7). Thus, it can be inferred that the coupling mechanism between BDC and $Ti_3C_2O_x$ involves the formation of strongly interacting coordination bonds between the reactive oxygen groups on the $Ti_3C_2O_x$ surface and the carboxyl groups on the ligand BDC.

To further support the above hypothesis, the XPS analysis was conducted to analyze the chemical state and surface elemental composition of BDC and T-BDC, as shown in Figs. 1f, 1g and Fig. S8. The high-resolution C 1s spectrum reveals that the binding energy at 284.72 eV and 289.16 eV corresponds to C-C and O-C=O in the carboxyl groups of BDC and T-BDC, respectively (Fig. 1f) [51]. Significantly, the high-resolution C 1s spectrum of T-BDC also reveals corresponding diffraction peaks of C=O, C-O, and Ti-C attributed to $Ti_3C_2O_x$. The binding energies of C=O (288.82→291.00 eV) and Ti-C (282.23→283.30 eV) notably shift higher compared to those of pure $Ti_3C_2O_x$ (Fig. 1f and Fig. S2), indicating a strong interaction between C=O on the surface of $Ti_3C_2O_x$ and the BDC. Meanwhile, Fig. 1g shows a downward shift in binding energies for the O-C=O (532.09→531.98 eV) and -OH (533.42→533.22 eV) peaks associated with BDC in T-BDC following pre-coupling with $Ti_3C_2O_x$. It is widely accepted that when atoms in a compound gain electrons (reduced valence state), the binding energy of the photoelectrons shifts to lower energy, and when they lose electrons (increased valence state), the binding energy of the photoelectrons shifts to higher energy. Thus, these results indicate that electrons transfer from C=O on the surface of $Ti_3C_2O_x$ to -COOH on BDC, resulting in an electronic rearrangement and the formation of a strong ligand interaction between $Ti_3C_2O_x$ and BDC. This is attributed to the ligand mechanism whereby the lone pair of electrons from C=O in $Ti_3C_2O_x$ enters the empty orbital of the carboxyl oxygen in BDC to form a coordination bond between $Ti_3C_2O_x$ and BDC. Furthermore, density functional theory (DFT) calculations were conducted to assess the potential for coordination bond formation between $Ti_3C_2O_x$ and the BDC ligand. The ground state energies of BDC, $Ti_3C_2O_x$, and T-BDC are depicted in Fig. 1h, which reveals that the binding energy of T-BDC is negative. This indicates that the pre-coupling process is a thermodynamically spontaneous reaction. Moreover, the bond length of O-C=O in the T-BDC is elongated from 1.22 to 1.24 after pre-coupling with $Ti_3C_2O_x$, which is consistent with the XRD finding. Electron location function (ELF) is a widely used and valuable method for analyzing electron delocalization and interatomic interactions within a system. Fig. 1i demonstrates a significant localization near the active oxygen group on the $Ti_3C_2O_x$ surface and the carboxyl oxygen of the ligand BDC, corroborating a robust interaction between these groups, in agreement with the experimental results.

3.2. Characterization of x% $Ti_3C_2O_x$/MIL-125(Ti) photocatalysts

The x% $Ti_3C_2O_x$/MIL-125(Ti) photocatalysts were synthesized directly using the pre-coupled ligand T-BDC (Scheme 1). The crystal morphology of pure MIL-125(Ti) and x% $Ti_3C_2O_x$/MIL-125(Ti) (x = 2, 5, 10, 15) was determined by XRD, and the results are presented in Fig. 2a and Fig. S9. The XRD analysis reveal that x% $Ti_3C_2O_x$/MIL-125(Ti) display diffraction peaks at 6.8°, 9.7°, 11.7°, 16.6°, 17.9°, 19.0° and 19.6°, without any noticeable deviation. It is consistent with the calculated MIL-125(Ti) and the previously reported literature [52–54], indicating the successful synthesis of the series of Ti-based MOFs (x% $Ti_3C_2O_x$/MIL-125(Ti)) using T-BDC ligands, without any damage to the
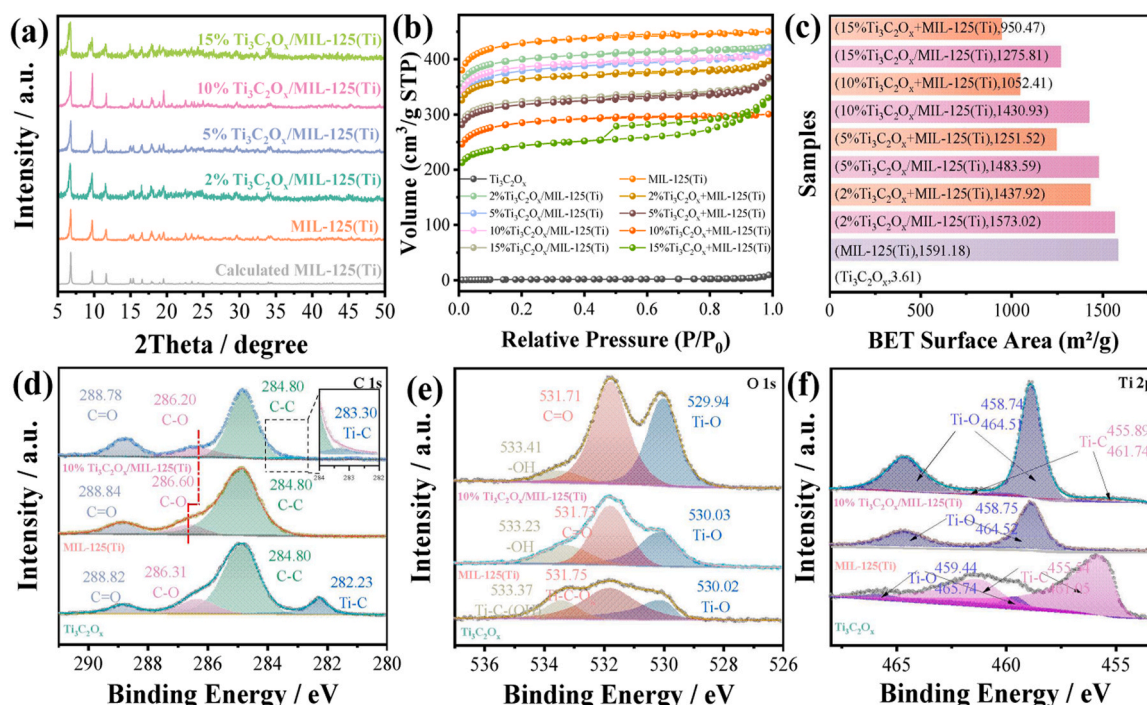
Fig. 2. Structure characterization of x% $Ti_3C_2O_x$/MIL-125(Ti) (a) XRD patterns, (b) Nitrogen adsorption-desorption isotherm, (c) corresponding specific surface area of the samples, and (d) high-resolution XPS spectra for C 1 s, (e) O 1 s, and (f) Ti 2p.

original crystal of pure MIL-125(Ti). The absence of observed diffraction peaks of $Ti_3C_2O_x$ could be attributed to its weak intensity, low content, and high dispersion [47]. As expected, the FT-IR signals of the x% $Ti_3C_2O_x$/MIL-125(Ti) photocatalysts are identical to the pure MIL-125 (Ti) (Fig. S10), further supporting the conclusion obtained from XRD analysis. To demonstrate that the ligand-bridged $Ti_3C_2O_x$/MIL-125(Ti) composites prepared using this ligand pre-coupling strategy did not sacrifice the specific surface area of the MOF matrix, Brunauer Emmett Teller (BET) characterization was performed. Figs. 2b and 2c display the BET specific surface area of $Ti_3C_2O_x$, MIL-125(Ti), x% $Ti_3C_2O_x$/MIL-125 (Ti), and $Ti_3C_2O_x$+MIL-125(Ti) (x = 2, 5, 10, 15). Notably, the BET specific surface area of x% $Ti_3C_2O_x$/MIL-125(Ti) (x = 2, 5, 10) remains above 1400 $m^2 \cdot g^{-1}$, similar to pure MIL-125(Ti) (1591.18 $m^2 \cdot g^{-1}$), whereas when $Ti_3C_2O_x$ continues to increase up to 15% $Ti_3C_2O_x$/-MIL-125(Ti), its specific surface area decreases to 1275.81 $m^2 \cdot g^{-1}$. In contrast, the BET surface area of $Ti_3C_2O_x$+MIL-125(Ti) obtained without pre-coupling process gradually decreases to 950.47 $m^2 \cdot g^{-1}$ as the $Ti_3C_2O_x$ content increases, all of which are lower than those of the corresponding x% $Ti_3C_2O_x$/MIL-125(Ti). All these results unambiguously demonstrate that $Ti_3C_2O_x$/MIL-125(Ti) photocatalyst has been successfully prepared with the T-BDC ligand.

The X-ray photoelectron spectroscopy (XPS) spectra were used to gain further insight into the variations in surface chemical states of 10% $Ti_3C_2O_x$/MIL-125(Ti). As anticipated, virgin MIL-125(Ti) and 10% $Ti_3C_2O_x$/MIL-125(Ti) consist of C, O, and Ti elements (Fig. S11). The high-resolution C 1 s XPS spectra of MIL-125(Ti) and 10% $Ti_3C_2O_x$/MIL-125(Ti) can be deconvolved into three and four absorption peaks, respectively, with the positions of the peaks emerging from small to large binding energy corresponding to Ti-C, C-C, C-O, and C=O, respectively (Fig. 2d). Noteworthily, the position of the C-O peak in 10% $Ti_3C_2O_x$/MIL-125(Ti) is shifted by 0.4 eV (286.60→286.20 eV) towards lower binding energy compared to pure MIL-125(Ti), which can be attributed to the interaction between the surface oxygen groups of $Ti_3C_2O_x$ and the carboxyl groups in the ligands. The high-resolution O 1 s XPS spectra of both samples in Fig. 2e can also be deconvolved into three absorption peaks, with the peaks belonging to Ti-O, C=O, and -OH from small to large, respectively. Likewise, the binding energies of -OH

and Ti-O in 10% $Ti_3C_2O_x$/MIL-125(Ti) also exhibit varying degrees of deviation compared to pure MIL-125(Ti) (Fig. 2e). The relative content of each element and the O-containing species (Table S2) in the sample were intuitively analyzed. The ratio of O-H in 10% $Ti_3C_2O_x$/MIL-125(Ti) decreased significantly from 47.64 to 5.77 (Table S2) compared to pure MIL-125(Ti), which is attributed to the fact that a carboxyl group in the ligand terephthalic acid is consumed to establish a tight coordination interaction with $Ti_3C_2O_x$ in the per-coupling process. The high-resolution Ti 2p spectrums in MIL-125(Ti) at 458.75 eV and 464.52 eV were ascribed to Ti 2p3/2 and Ti 2p1/2 of Ti-O, respectively (Fig. 2f). In contrast, the Ti 2p spectra in 10% $Ti_3C_2O_x$/MIL-125(Ti) can be deconvolved into four absorption peaks. The peaks at 458.74 eV and 464.51 eV correspond to Ti 2p3/2 and Ti 2p1/2 of Ti-O, respectively, while the peaks at 455.89 eV and 461.74 eV correspond to Ti 2p3/2 and Ti 2p1/2 of Ti-C in $Ti_3C_2O_x$, respectively. The aforementioned results confirm that the carboxyl groups in the terephthalic acid ligand establish strong interactions between $Ti_3C_2O_x$ and MIL-125(Ti) through coordination bonds.

The morphology and microstructure of $Ti_3C_2O_x$, MIL-125(Ti), 10% $Ti_3C_2O_x$/MIL-125(Ti) and 10% $Ti_3C_2O_x$+MIL-125(Ti) samples were further invested. The scanning electron microscopy (SEM) images of MIL-125(Ti) were displayed in Figs. 3a and 3b, exhibiting a three-dimensional crystal block with smooth surface and edges with particle size of 2 ~ 5 μm. The particle size of 10% $Ti_3C_2O_x$/MIL-125(Ti) increased slightly compared to the pure MIL-125(Ti) due to the enlarged in T-BDC after functionalization of $Ti_3C_2O_x$. The $Ti_3C_2O_x$ was anchored onto the surface of MIL-125(Ti), resulting in a rough surface that facilitates the exposure of active sites and surface catalytic reactions [55]. The edges of the material transformed into a three-dimensional disc-like structure resembling a tablet (Figs. 3c and 3d). In contrast, $Ti_3C_2O_x$+MIL-125(Ti) obtained without pre-coupling process exhibited a structure similar to pure MIL-125, with no significant presence of $Ti_3C_2O_x$ observed (Figs. 3e and 3f). For comparison, SEM and TEM images of $Ti_3C_2O_x$ are presented in Figs. 3g and 3h, depicting the aggregation of small-sized 2D sheets that are consistent with those shown in Figs. 3c and 3d. The microstructure of 10% $Ti_3C_2O_x$/MIL-125(Ti) was further probed by the high-resolution transmission electron microscopy
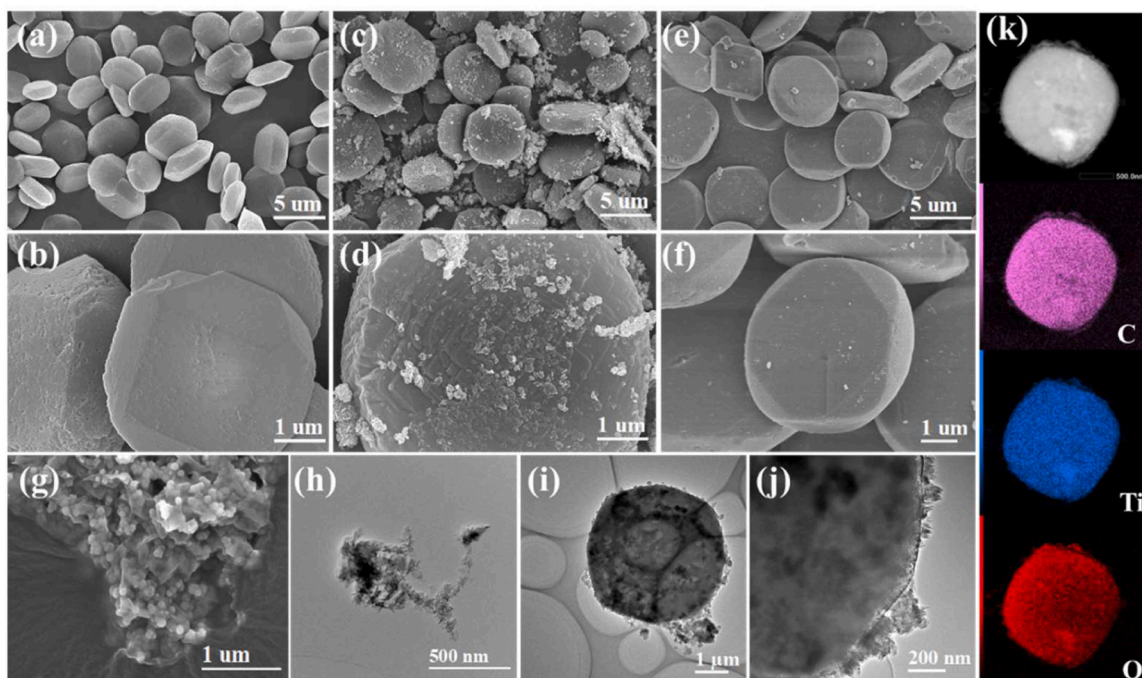
**Fig. 3.** SEM images of (a, b) MIL-125(Ti), (c, d) 10% $Ti_3C_2O_x$/MIL-125(Ti), (e, f) 10% $Ti_3C_2O_x$+MIL-125(Ti), (g) $Ti_3C_2O_x$; TEM images of (h) $Ti_3C_2O_x$, (i, j) 10% $Ti_3C_2O_x$/MIL-125(Ti); (k) High Angle annular dark field (HAADF) and corresponding EDX elemental mapping images of C, Ti, O for 10% $Ti_3C_2O_x$/MIL-125(Ti).

(HRTEM) image (Figs. 3i and 3j). The signal intensity of the 10% $Ti_3C_2O_x$/MIL-125(Ti) tablet varies, with the weaker portion potentially resulting from $Ti_3C_2O_x$ adhered to the surface of MIL-125(Ti) and/or from the presence of $Ti_3C_2O_x$ within the interior of the three-dimensional tablet. Furthermore, a significant amount of $Ti_3C_2O_x$ can be observed attached to the edge of MIL-125(Ti) (Fig. 3j). The uniform dispersion of C, Ti, and O element mapping in 10% $Ti_3C_2O_x$/-MIL-125(Ti) (Fig. 3k) was observed by high-angle annular dark-field scanning transmission electron microscopy (HAADF-STEM), which further confirmed the successful synthesis of $Ti_3C_2O_x$/MIL-125(Ti) composites.

3.3. Performance and mechanism of photocatalytic ammonia synthesis by x% $Ti_3C_2O_x$/MIL-125(Ti)

The dinitrogen photofixation activity over x% $Ti_3C_2O_x$/MIL-125(Ti) has been investigated to disclose the role of $Ti_3C_2O_x$ and to determine its optimal content (Fig. 4). The ammonia produced in the control experiment (no light, no photocatalysts, or no dinitrogen) for all the catalysts was negligible, and pure $Ti_3C_2O_x$ has no ammonia synthesis activity (Figs. S12-S13). Fig. 4a exhibits that the NH_4^+ generation rate of pure MIL-125(Ti) without any co-catalyst was poor due to the low charge transformation efficiency, whereas the rate of x% $Ti_3C_2O_x$/MIL-125(Ti)
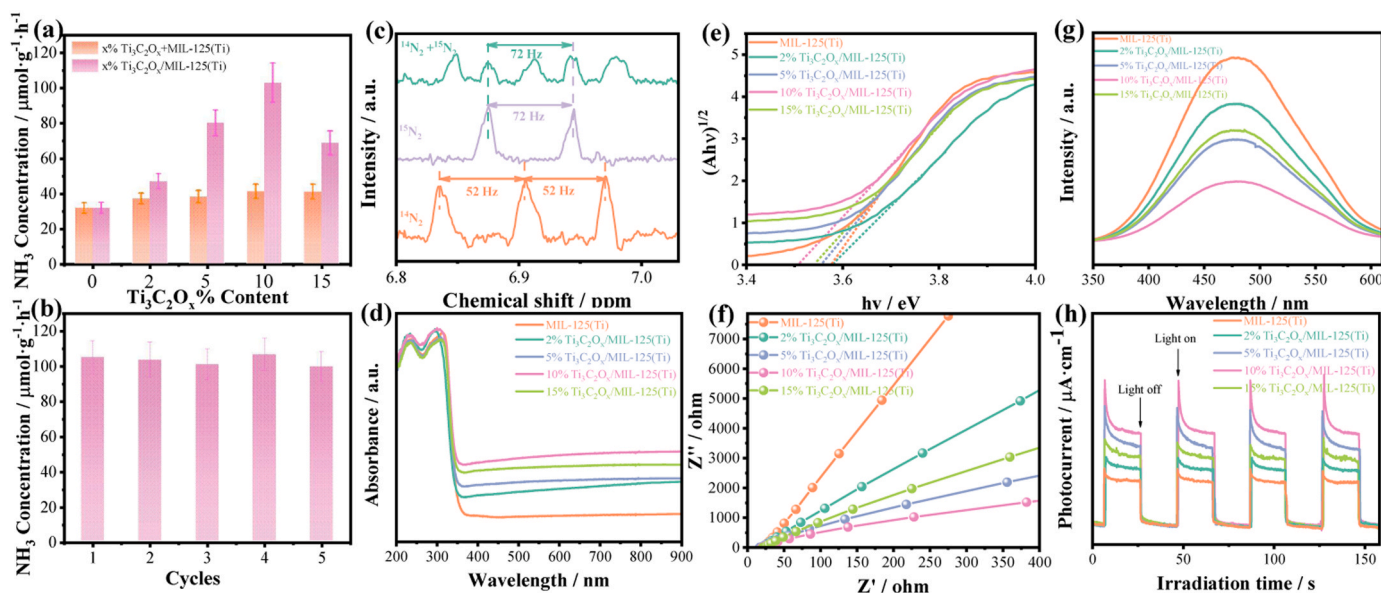
Fig. 4. (a) Photocatalytic ammonia synthesis rates of x% $Ti_3C_2O_x$/MIL-125(Ti) and x% $Ti_3C_2O_x$+MIL-125(Ti); (b) cyclic operation of 10% $Ti_3C_2O_x$/MIL-125(Ti); (c) ^{1}H NMR spectra of 10% $Ti_3C_2O_x$/MIL-125(Ti) fed by $^{14}N_2$, $^{15}N_2$, and $^{14}N_2$ +$^{15}N_2$ (1:1 vol%); (d) UV−vis DRS spectra, (e) Tauc plots, (f) EIS spectra, and (g) Room-temperature steady-state PL spectra of x% $Ti_3C_2O_x$/MIL-125(Ti), and (h) Transient photocurrent responses of x% $Ti_3C_2O_x$/MIL-125(Ti).

with different contents of $Ti_3C_2O_x$ was significantly enhanced. The NH_4^+ generation rate of x% $Ti_3C_2O_x$/MIL-125(Ti) increases first and then decreases with the increase of $Ti_3C_2O_x$ content. Accordingly, the highest NH_4^+ generation rate (103.02 $\mu mol \cdot g_{cat}^{-1} \cdot h^{-1}$) is achieved with the optimal $Ti_3C_2O_x$ content (10% $Ti_3C_2O_x$/MIL-125(Ti)), which is 3.25 times that of pure MIL-125(Ti) (31.68 $\mu mol \cdot g_{cat}^{-1} \cdot h^{-1}$) and also surpasses many previously reported MOF-based photocatalysts (Table S3). Gas chromatography was employed to determine the product of the gas phase in the reactor, which revealed the presence of oxygen but not hydrogen (Fig. S14). This indicates that oxygen is the product in the valence band, and the competing hydrogen precipitation reaction in the conduction band is effectively suppressed. Conversely, the NH_4^+ yield of x% $Ti_3C_2O_x$+MIL-125(Ti) obtained without pre-coupling process was not substantially enhanced, suggesting that the ligand molecular bridge established by pre-coupling technique between MIL-125(Ti) and $Ti_3C_2O_x$ plays a key role in improving nitrogen photofixation activity. Furthermore, 10% $Ti_3C_2O_x$/MIL-125(Ti) exhibits excellent reusability and sustainability in five cycles (Fig. 4b) as well as in long time stability test (Fig. S15), and the XRD patterns (Fig. S16) show negligible changes in crystal shape, confirming the stability of the catalyst. In order to provide additional confirmation regarding the source of ammonia produced through N_2 fixation, experiments involving the labeling of $^{15}N_2$ isotopes were conducted, utilizing pure $^{15}N_2$ and 50 vol% $^{15}N_2$ as the purge gas. As seen in Fig. 4c, the ^1H NMR signals only exhibit triplet symmetric signals of $^{14}NH_4^+$ with spacing of 52 Hz in the $^{14}N_2$ atmosphere, doublet signal of $^{14}NH_4^+$ with spacing of 72 Hz in $^{15}N_2$ atmosphere, while the curve containing 50 vol% $^{15}N_2$ gas display both the typical triplets for $^{14}NH_4^+$ and doublets for $^{15}NH_4^+$. These results convincingly verified that the detected ammonia is derived from N_2 gas.

Fig. 4d displays the UV–vis diffuse reflectance spectra (UV–vis DRS) of x% $Ti_3C_2O_x$/MIL-125(Ti), unveiling their light harvesting performance. Compared with pure MIL-125(Ti), x% $Ti_3C_2O_x$/MIL-125(Ti) exhibits enhanced optical absorption in both ultraviolet and visible regions, attributed to the strong absorption of $Ti_3C_2O_x$ across the full spectrum. In general, the band gap of semiconductor materials can be calculated by the Kubelka-Munk formula (Eq. 1), and the relationship Tauc plots between $(Ah\nu)^{1/2}$ and $(h\nu-E_g)$ was displayed in Fig. 4e. It was found that the band gap of the 10% $Ti_3C_2O_x$/MIL-125(Ti) catalyst was slightly reduced compared to that of the pure MIL-125(Ti), but it was still adequate for hydrolysis dissociation and ammonia synthesis (Fig. S17).

$$\alpha h\nu = A(h\nu - E_g)n \tag{1}$$

Where α, H, ν, A, n, and E_g are optical absorption coefficient, Planck constant, optical frequency, measured absorbance, 2 (indirect transition), and band gap value, respectively.

Meanwhile, electrochemical impedance spectroscopy (EIS) photoluminescence (PL) emission spectrum and photocurrent (PC) response measurements were conducted to further explore the photoelectric properties and charge transfer capabilities at the interface of the photocatalysts. The slope of EIS patterns of x% $Ti_3C_2O_x$/MIL-125(Ti) was lower than that of pure MIL-125(Ti), indicating a decreased interfacial electron transport resistance (Fig. 4f). Additionally, the PL emission peaks of MIL-125(Ti) and x% $Ti_3C_2O_x$/MIL-125(Ti) were obtained with an excitation wavelength of 273 nm (Fig. 4g). The intensity of the PL emission peaks in x% $Ti_3C_2O_x$/MIL-125(Ti) (x = 2, 5, 10, 15) is significantly decreased, indicating that $Ti_3C_2O_x$ acts as co-catalysts prevent the recombination of photogenerated electron-hole pairs. Similarly, the photocurrent response density of x% $Ti_3C_2O_x$/MIL-125(Ti) increases first and then decreases with increasing $Ti_3C_2O_x$ content (Fig. 4h). Surprisingly, all those kinetic data (EIS, PL, PC) are consistent with the results of photocatalytic ammonia synthesis activity. These results not only verifies that $Ti_3C_2O_x$, as a co-catalyst, enhances the photochemical properties and facilitates the migration and separation of charge carriers but also further demonstrates that 10% $Ti_3C_2O_x$/MIL-125(Ti) exhibits

the highest splitting efficiency of the photoinduced carriers.

To further verify the role of the ligand molecular bridge in charge transportability and separation, the surface charge separation efficiency ($\eta_{surface}$) of MIL-125(Ti), 10% $Ti_3C_2O_x$/MIL-125(Ti) and 10% $Ti_3C_2O_x$+MIL-125(Ti) is studied through the addition of fast electrons scavenger (H_2O_2) into electrolyte [56,57] to further insight into the coordination bonds between $Ti_3C_2O_x$ and MIL-125(Ti) contribute significantly to photogenerated electron-hole pair separation. When H_2O_2 is added to the electrolyte solution, the surface charge transfer becomes extremely fast and the η_{trans} approximately reaches 100%. Thus, the charge separation efficiency in the surface $\eta_{surface}$ can be defined by the undermentioned Eq. 2.

$$\eta_{surface} = \frac{J_{H_2O}}{J_{H_2O_2}} \tag{2}$$

Where J_{H2O} and J_{H2O2} are the photocurrent density in the Na_2SO_4 aqueous solution without and with adding H_2O_2, respectively.

Fig. 5a displays that the photocurrent of MIL-125(Ti) raises from 0.134 $\mu A\ cm^{-2}$ to 0.456 $\mu A\ cm^{-2}$ after adding H_2O_2 into the electrolyte solution, while the photogenerated current of 10% $Ti_3C_2O_x$/MIL-125(Ti) and 10% $Ti_3C_2O_x$+MIL-125(Ti) increases from 0.268 $\mu A\ cm^{-2}$ to 0.534 $\mu A\ cm^{-2}$ and from 0.119 $\mu A\ cm^{-2}$ to 0.482 $\mu A\ cm^{-2}$, respectively. This phenomenon is attributed to that H_2O_2 is much more easily reduced than H_2O. Accordingly, the $\eta_{surface}$ of MIL-125(Ti), 10% $Ti_3C_2O_x$/MIL-125(Ti) and 10% $Ti_3C_2O_x$+MIL-125(Ti) is calculated to be 29.6%, 50.2%, and 24.7% respectively. This result reveals that the surface electron transfer efficiency can be improved only in the presence of ligand molecular bridge between $Ti_3C_2O_x$ and MIL-125(Ti).

Time-resolved photoluminescence (TRPL) was also conducted to explore the electron transportability behavior of MIL-125(Ti), 10% $Ti_3C_2O_x$/MIL-125(Ti) and 10% $Ti_3C_2O_x$+MIL-125(Ti). According to Fig. 5b and Table S4, the average fluorescence lifetime of MIL-125(Ti), 10% $Ti_3C_2O_x$/MIL-125(Ti) and 10% $Ti_3C_2O_x$+MIL-125(Ti) are 1.72, 2.90 and 1.89 ns, respectively, indicating that only constructing ligand molecular bridge between $Ti_3C_2O_x$ and MIL-125(Ti) will lengthen the lifetime of the photogenerated carriers. Noteworthily, these phenomena are in good agreement with the results of the performance of dinitrogen photofixation. Figs. 5c and 5d shows the two-dimensional and three-dimensional AFM morphology of 10% $Ti_3C_2O_x$/MIL-125(Ti), exhibiting tablet-like crystal block with co-catalyst $Ti_3C_2O_x$ attached at the edges, in agreement with SEM. Intuitively, the introduction of kelvin probe force microscopy (KPFM) based on atomic force microscopy (AFM) for simultaneous region-specific topographic imaging and SPV signal measurements to probe photo-generated charge transfer and segregation of 10% $Ti_3C_2O_x$/MIL-125(Ti) under dark and illuminating, respectively. Upon illumination, the color change is more noticeable than in the dark, indicating a greater surface potential difference (Fig. 5e). Fig. 5 f shows the height and surface potential of 10% $Ti_3C_2O_x$/MIL-125(Ti) under dark and irradiation conditions along the red line in Figs. 5c and 5e. Under irradiation conditions, there is a significant surface potential difference (Δ = 1.48 eV) at the interface of MIL-125(Ti) and $Ti_3C_2O_x$ (shaded area in Fig. 5 f) that can be attributed to the unidirectional transport of electrons from MIL-125(Ti) to $Ti_3C_2O_x$, while there is no significant potential difference in the dark state. These findings suggest that the photogenerated electrons are easily transferred from MIL-125(Ti) to $Ti_3C_2O_x$ surface through the ligand molecular bridge, which greatly improves the transfer and separation behavior of photogenerated carriers from MOFs.

To evaluate the universality of the ligand pre-coupling strategy, five other commonly investigated MOFs (UiO-66(Zr), MIL-101(Fe), Cu-BDC, UiO-66(Ce), MOF-5) were synthesized with ligand BDC and precoupling T-BDC. The XRD patterns of the samples with T-BDC are consistent with those of the pristine MOFs with BDC ligand (Figs. S18-S22), indicating that they have the same main frame structure as the original MOFs. As shown in Fig. 6, the surface charge separation
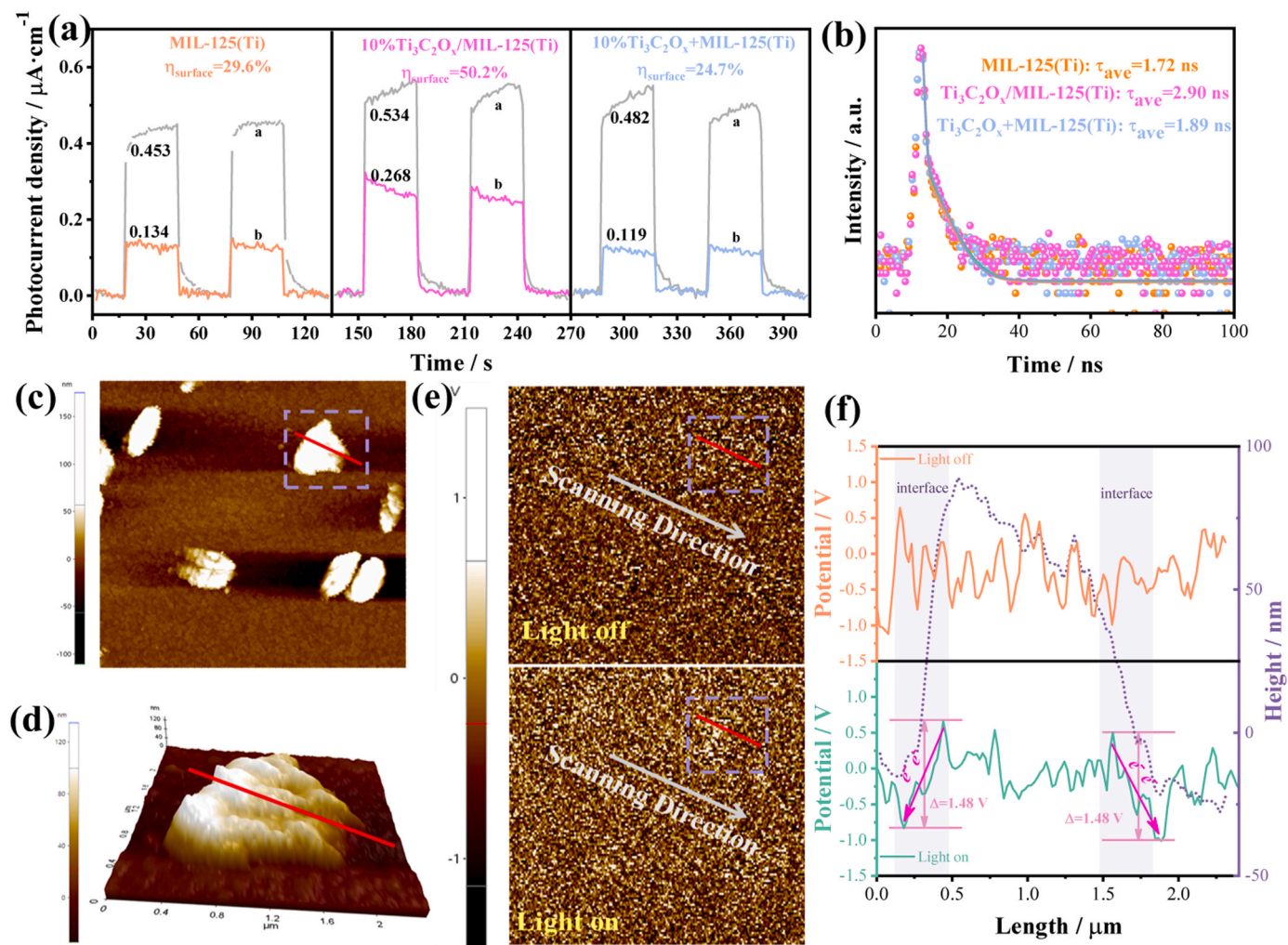
Fig. 5. (a) The photocurrent response of MIL-125(Ti), 10% $Ti_3C_2O_x$/MIL-125(Ti) and 10% $Ti_3C_2O_x$+MIL-125(Ti) without and with adding H_2O_2 into electrolyte (a: adding H_2O_2; b: no H_2O_2), and (b) time-resolved photoluminescence spectroscopy (TRPL), (c-d) two-dimensional and three-dimensional AFM morphology, (e) KPFM surface potential images, and (f) the corresponding height and surface potential curve along line in the inset of part in the dark and illumination of 10% $Ti_3C_2O_x$/MIL-125(Ti).

efficiencies ($\eta_{surface}$) of the five $Ti_3C_2O_x$/MOFs are higher than those of the corresponding pure MOFs after $Ti_3C_2O_x$ pre-coupling, among which UiO-66(Zr), MIL-101(Fe), Cu-BDC, UiO-66(Ce), and MOF-5 have been enhanced by a factor of 2.24, 1.64, 1.43, 2.01, and 1.2, respectively. This result reveals that they have largely improved photogenerated charge transportability and separation upon the pre-coupling with $Ti_3C_2O_x$. Thus, the ligand pre-coupling strategy has good universality in improving electron transfer and separation between interfaces of MXene/MOFs heterojunctions by the pre-construction of coordination bond between terephthalic acid and cocatalyst as a bridge for charge transport.

Time-dependent in situ diffuse reflectance infrared Fourier-transform spectroscopy (DRIFTS) was employed to track potential intermediate products throughout the photocatalytic NRR process. As shown in Fig. 7, the adsorption bands at 3550, 2971, 2895, 2362, 2338, and 1100–1700 cm^{-1} gradually increase with the irradiation time from 0 to 60 min under wet N_2 atmosphere. Specifically, the bands at 2362 and 2338 cm^{-1} arise from characteristics of the chemisorbed N_2 species [58]. The broad absorption ranging from 3000 to 3700 cm^{-1} and the peak location at 1643 cm^{-1} can be assigned to the ν(O-H) stretching mode and σ(O-H) bending mode due to the adsorbed water [59,60]. The sharp band at 3550 cm^{-1} was ascribed to the ν(N-H) stretching mode, while the two peaks at 1610 and 1566 cm^{-1} were assigned to the σ(N-H)

bend mode [61,62]. Furthermore, the weak peak at 1296 and the bands at 2971 and 2895 cm^{-1} were attributed to the wagging mode of NH_2 and the characteristic absorption of NH_4^+ [63,64]. Additionally, sharp peaks appearing at 1496 and 1157 cm^{-1} arose from HN=NH and H_2N-NH_2, respectively [55]. The above results and analysis provide powerful evidence to propose a possible symmetric side-on mechanism.

The first principles calculations were employed to deep insight into the influence of ligand molecular bridge on the adsorption activation of N_2 molecule. The optimized configuration and the difference charge density of 10% $Ti_3C_2O_x$/MIL-125(Ti) are displayed in Fig. S23 and Figs. 8a-8b. Fig. 8a and Fig. S24 show that significant charge transfer occurs at the interface between $Ti_3C_2O_x$ and MIL-125(Ti), with electrons (yellow area) primarily transferring to the $Ti_3C_2O_x$ layer via the ligand molecular bridge. Additionally, the variation curve in Fig. 8b of the mean differential charge density in the z direction provides additional evidence of electron transfer from MIL-125(Ti) to the $Ti_3C_2O_x$ layer, which confirms that $Ti_3C_2O_x$ can function as an electron collector by effectively capturing electrons through the ligand molecular bridge. These findings are well consistent with KPFM results. The charge density difference of 10% $Ti_3C_2O_x$/MIL-125(Ti) with the adsorption of N_2 is further calculated (Fig. 8c). It is observed that significant electron exchange and transfer occur at the interface between the $Ti_3C_2O_x$ and MIL-125(Ti) with the N_2 molecule and that the two N atoms exhibit opposite

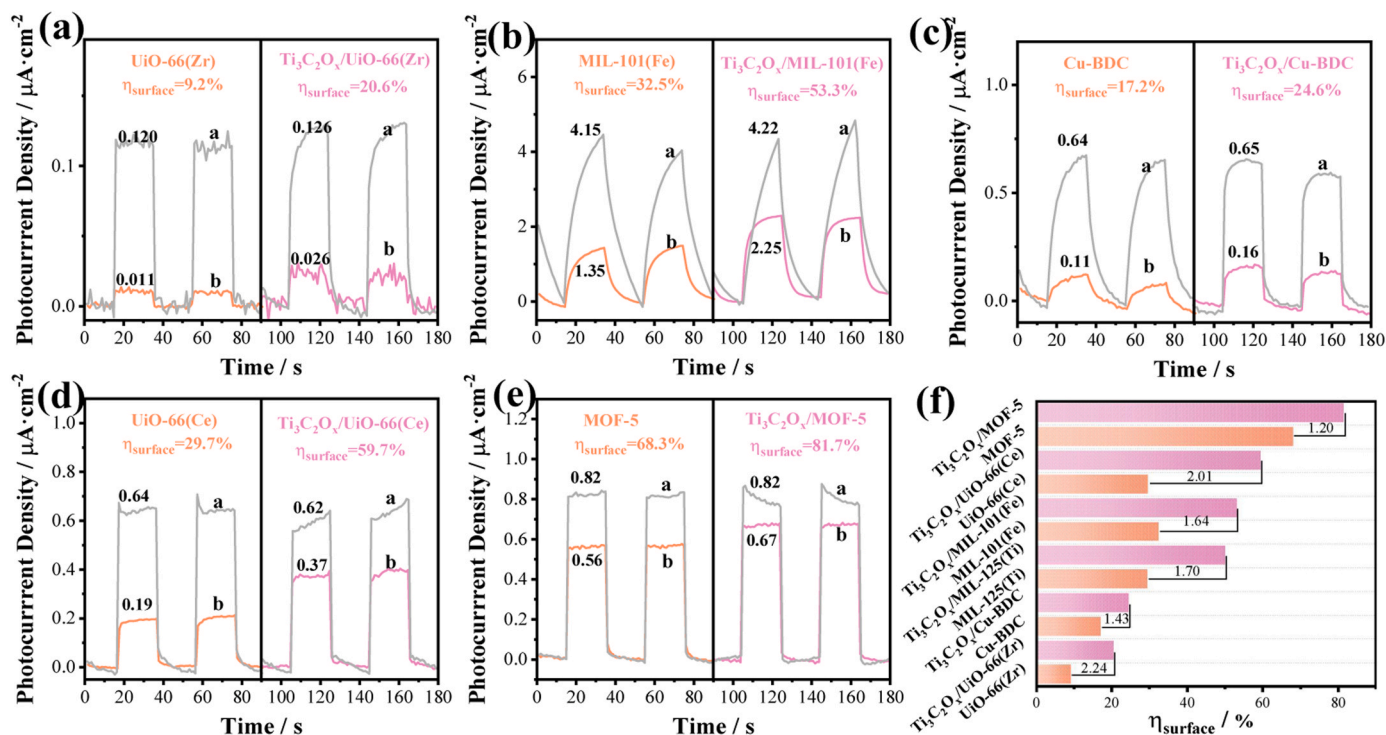**Fig. 6.** The photocurrent response of (a) UiO-66(Zr) and Ti$_3$C$_2$O$_x$/UiO-66(Zr), (b) MIL-101(Fe) and Ti$_3$C$_2$O$_x$/MIL-101(Fe), (c) Cu-BDC and Ti$_3$C$_2$O$_x$/Cu-BDC, (d) UiO-66(Ce) and Ti$_3$C$_2$O$_x$/UiO-66(Ce), (e) MOF-5 and Ti$_3$C$_2$O$_x$/MOF-5 without and with adding H$_2$O$_2$ into electrolyte (a: adding H$_2$O$_2$; b: no H$_2$O$_2$); (f) Histogram of surface charge separation efficiency η$_{surface}$ distribution.
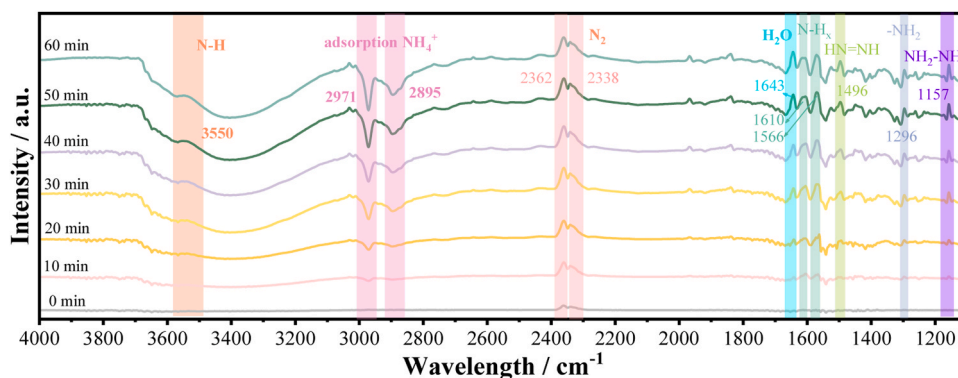

Fig. 7. In-situ FTIR spectra recorded during the photocatalytic ammonia synthesis over 10% Ti$_3$C$_2$O$_x$/MIL-125(Ti).

electrical properties. These results agree well with the "acceptance-donation" process for activating N$_2$. To provide deep insights into the *N$_2$ activation degree the integrated-crystal orbital Hamilton population (ICOHP) [65,66] analysis of N≡N bond was performed (Fig. 8d). In general, for the value of ICOHP, a more negative value corresponds to the stronger bonding [67]. Obviously, the ICOHP increased from − 22.91 for free N$_2$ to − 8.84 for *N$_2$, demonstrating that N$_2$ molecules adsorbed on 10% Ti$_3$C$_2$O$_x$/MIL-125(Ti) were effectively activated. Moreover, the partial density of states (Fig. S25) and Bader charges results (Table S5) for the *N$_2$ and its neighboring atoms align with the results of COHP analysis. These results suggest that the ligand molecular bridge weakens the energy barrier for electron transfer at the interface of Ti$_3$C$_2$O$_x$ and MIL-125(Ti), increases the electron cloud density at the interface, and thus facilitates the activation of nitrogen molecules.

The nitrogen reduction reaction (NRR) process, specifically the hydrogenation of nitrogen molecules (N$_2$), can occur through two different pathways. Accordingly, the Gibbs free energy of the distal and the alternating pathways of 10% Ti$_3$C$_2$O$_x$/MIL-125(Ti) are calculated,

respectively (Fig. 8e). The initial step of both pathways involves the formation of NNH (*N$_2$ + H$^+$ + e$^-$ = *NNH) and exhibits a favorable Gibbs free-energy change (ΔG) of 0.981 eV. However, the subsequent hydrogenation steps differ for the two pathways. In the alternating pathway, the second hydrogenation step (*NNH + H$^+$ + e$^-$ = *HNNH) has a ΔG of 0.801 eV, while the distal pathway shows a ΔG of 1.299 eV for its second hydrogenation step (*NNH + H$^+$ + e$^-$ = *NNH$_2$). The disparity becomes more pronounced in the following hydrogenation step. In the distal pathway, the formation of *NNH$_3$ (*NNH$_2$ + H$^+$ + e$^-$ = *NNH$_3$) encounters the highest energy barrier of 1.627 eV, indicating that it is the rate-determining step in this pathway. In contrast, the alternating pathway (*HNNH + H$^+$ + e$^-$ = *HNNH$_2$) has a significantly lower uphill energy barrier of − 0.456 eV. Moreover, the subsequent hydrogenation step in the alternating pathway (*HNNH$_2$ + H$^+$ + e$^-$ = *H$_2$NNH$_2$), displays an even lower uphill energy barrier of − 0.474 eV. Furthermore, analyzing the changes in the N-N bond length across different reaction pathways can help identify the N$_2$ hydrogenation pathway. According to Fig. 8f, the N-N bond length undergoes
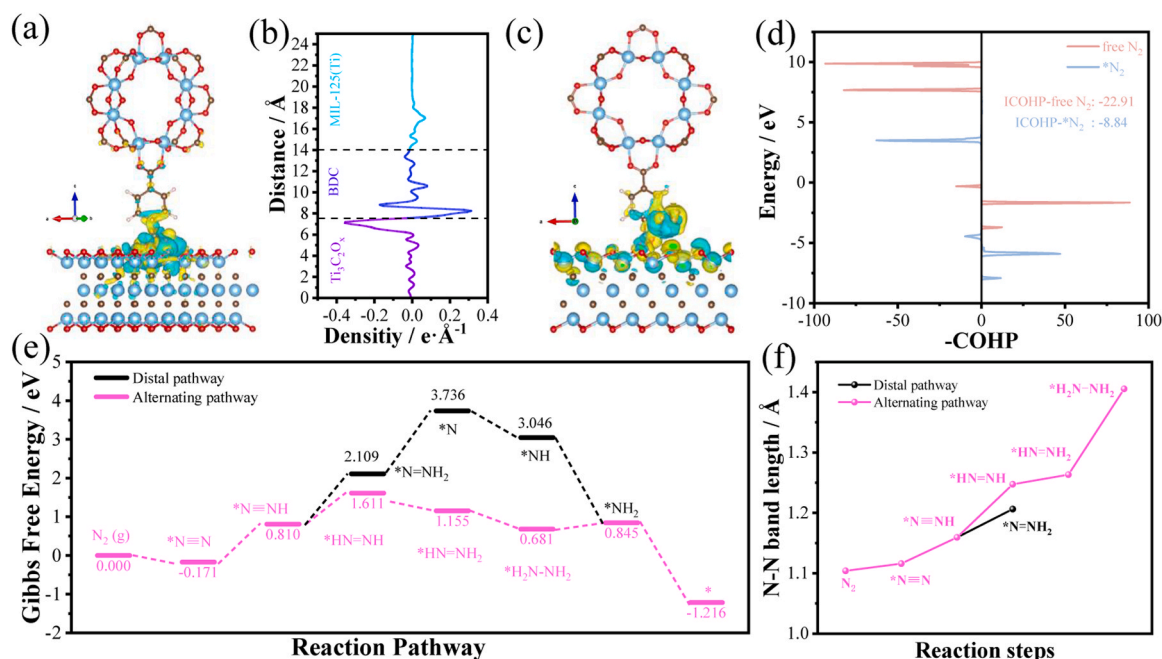
Fig. 8. The charge density difference of (a) 10% $Ti_3C_2O_x$/MIL-125(Ti), (b) corresponding 2D curve in the z direction, and (c) 10% $Ti_3C_2O_x$/MIL-125(Ti) after absorbed of N_2 (cyan and yellow represent charge loss and charge accumulation, respectively); (d) the crystal orbital Hamilton population (COHP) between N≡N of free N_2 and *N_2 on 10% $Ti_3C_2O_x$/MIL-125(Ti); (e) free-energy diagram for alternating and distal pathways on 10% $Ti_3C_2O_x$/MIL-125(Ti), and (f) N≡N bond length changes with the reaction process.

elongation from 1.10 Å (pure N_2) to 1.21 Å (N-NH_2) along the distal reaction pathway. Conversely, the N-N bond length increases further to 1.41 Å (H_2N-NH_2) along the alternating pathway, which favors the N_2 hydrogenation process. Collectively, these experimental and computational findings synergistically provide evidence that the photocatalytic NRR of 10% $Ti_3C_2O_x$/MIL-125(Ti) predominantly follows the alternating reaction pathway.

4. Conclusions

In summary, a novel ligand pre-coupling strategy was developed to create a method of preparing organic ligand bridged MXene/metal-organic frameworks composites. The prepared MXene/MOFs heterojunctions exhibit significant improvement in the separation of photogenerated charge carriers while preserving most of their original active surface, benefiting from the forming coordination bonds between the reactive groups on the $Ti_3C_2O_x$ surface and the carboxyl groups on the ligand BDC. Furthermore, experiments and calculations demonstrate that the ligand serves as molecule bridge connecting MIL-125(Ti) and MXene, establishing a unidirectional electron transport channel that facilitates the activation of nitrogen molecules across the interface and subsequent synthesis of ammonia via an alternating pathway. Under the above advantages, the synthesized $Ti_3C_2O_x$/MIL-125(Ti) composites displayed an excellent ammonia yield of 103.02 μmol·g_{cat}^{-1}·h^{-1}, which is 3.25 times higher than that of pure MIL-125(Ti), in pure water system under simulated solar irradiation. This strategy has demonstrated extensive applicability in constructing ligand bridging MXene/MOFs heterojunctions for six common MOFs (MIL-125(Ti), MOF-5, UIO-66 (Zr), UIO-66(Ce), MIL-101(Fe), Cu-BDC) with BDC ligands. This report offers new insights into developing novel co-catalysts/MOFs heterojunctions photocatalysts to overcome the high interfacial energy barrier while preserving the active sites of the host.

CRediT authorship contribution statement

Gao Xiaoming: Software. **Jian Xuan:** Resources, Software. **Li Rui:**

Funding acquisition. **Wang Zhongde:** Supervision, Writing – review & editing. **Zhang Xiaochao:** Resources. **Guo Lijun:** Resources. **Wang Yunfang:** Validation. **Wang Yawen:** Supervision. **Fan Caimei:** Funding acquisition, Visualization, Writing – review & editing. **Li Feifei:** Formal analysis, Software. **Liu Jianxin:** Conceptualization, Funding acquisition, Project administration, Supervision, Writing – review & editing. **Shen Zhengfeng:** Conceptualization, Data curation, Investigation, Writing – original draft.

Declaration of Competing Interest

The authors declare that they have no known competing financial interests or personal relationships that could have appeared to influence the work reported in this paper.

Data availability

Data will be made available on request.

Acknowledgements

Appendix A. Supporting information

Supplementary data associated with this article can be found in the online version at doi:10.1016/j.apcatb.2024.123732.

References

[1] X.L. Xue, R.P. Chen, C.Z. Yan, P.Y. Zhao, Y. Hu, W.J. Zhang, S.Y. Yang, Z. Jin, Review on photocatalytic and electrocatalytic artificial nitrogen fixation for

ammonia synthesis at mild conditions: advances, challenges and perspectives, Nano Res. 12 (2019) 1229–1249.

[2] X.J. Zhu, S.Y. Mou, Q.L. Peng, Q. Liu, Y.L. Luo, G. Chen, S.Y. Gao, X.P. Sun, Aqueous electrocatalytic N_2 reduction for ambient NH_3 synthesis: recent advances in catalyst development and performance improvement, J. Mater. Chem. A 8 (2020) 1545–1556.

[3] S.L. Zhao, X.Y. Lu, L.Z. Wang, J.L. Gale, R. Amal, Carbon-based metal-free catalysts for electrocatalytic reduction of nitrogen for synthesis of ammonia at ambient conditions, Adv. Mater. 31 (2019) 1805367.

[4] A.M. Liu, M.F. Gao, X.F. Ren, F.N. Meng, Y.N. Yang, Q.Y. Yang, W.X. Guan, L. G. Gao, X.Y. Liang, T.L. Ma, A two-dimensional Ru@MXene catalyst for highly selective ambient electrocatalytic nitrogen reduction, Nanoscale 12 (2020) 10933–10938.

[5] Y.T. Gong, J.Z. Wu, M. Kitano, J.J. Wang, T.N. Ye, J. Li, Y. Kobayashi, K. Kishida, H. Abe, Y. Niwa, H.S. Yang, T. Tada, H. Hosono, Ternary intermetallic LaCoSi as a catalyst for N_2 activation, Nat. Catal. 1 (2018) 178–185.

[6] S.L. Foster, S.I.P. Bakovic, R.D. Duda, S. Maheshwari, R.D. Milton, S.D. Minteer, M. J. Janik, J.N. Renner, L.F. Greenlee, Catalysts for nitrogen reduction to ammonia, Nat. Catal. 1 (2018) 490–500.

[7] E.S. Mostafa, K. Shinji, Recent advances in ammonia synthesis technologies: toward future zero carbon emissions, Int. J. Hydrog. Energy 48 (2023) 11237–11273.

[8] V.K. Elham, H.Y. Aziz, G. Srabanti, Visible-light-induced nitrogen photofixation ability of g-C_3N_4 nanosheets decorated with MgO, Nanopart., J. Ind. Eng. Chem. 84 (2020) 185–195.

[9] B.T. Sun, P.Y. Qiu, Z.Q. Liang, Y.J. Xue, X.L. Zhang, L. Yang, H.Z. Cui, J. Tian, The fabrication of 1D/2D CdS nanorod@Ti_3C_2 MXene composites for good photocatalytic activity of hydrogen generation and ammonia synthesis, Chem. Eng. J. 406 (2021) 127177.

[10] J. Li, H. Li, G.M. Zhan, L.Z. Zhang, Solar water splitting and nitrogen fixation with layered bismuth oxyhalides, Acc. Chem. Res. 50 (2017) 112–121.

[11] Q. Han, C.B. Wu, H.M. Jiao, R.Y. Xu, Y.Z. Wang, J.J. Xie, Q. Guo, J.W. Tang, Rational design of high-concentration Ti^{3+} in porous carbon-doped TiO_2 nanosheets for efficient photocatalytic ammonia synthesis, Adv. Mater. 33 (2021) 2008180.

[12] N. Zhang, A. Jalil, D.X. Wu, S.M. Chen, Y.F. Liu, C. Gao, W. Ye, Z.M. Qi, H.X. Ju, C. M. Wang, X.J. Wu, L. Song, J.F. Zhu, Y.J. Xiong, Refining defect states in $W_{18}O_{49}$ by Mo doping: a strategy for tuning N_2 activation towards solar-driven nitrogen fixation, J. Am. Chem. Soc. 140 (2018) 9434–9443.

[13] K.L. Li, S. Chen, H.F. Wang, F. Wang, Plasma-assisted ammonia synthesis over Ni/ LaOF: Dual active centers consisting of oxygen vacancies and Ni, Appl. Catal. A Gen. 650 (2023) 118983.

[14] Y.H. He, X. Chen, Z.S. Wu, Q.W. Xue, F. Tian, In situ fabrication of N-doped $Ti_3C_2T_x$-MXene-modified BiOBr Schottky heterojunction with high photoelectron separation efficiency for enhanced photocatalytic ammonia synthesis, J. Alloy. Compd. 969 (2023) 172470.

[15] G.N. Schrauzer, T.D. Guth, Photolysis of water and photoreduction of nitrogen on titanium dioxide, J. Am. Chem. Soc. 99 (1977) 7189–7193.

[16] Y.T. Qian, F.F. Zhang, H. Pang, A review of MOFs and their composites-based photocatalysts: synthesis and applications, Adv. Funct. Mater. 31 (2021) 2104231.

[17] R. Jaryal, R. Kumar, S. Khullar, Mixed metal-metal organic frameworks (MM-MOFs) and their use as efficient photocatalysts for hydrogen evolution from water splitting reactions, Coord. Chem. Rev. 464 (2022) 214542.

[18] G. Cai, P. Yan, L. Zhang, H.C. Zhou, H.L. Jiang, Metal-organic framework-based hierarchically porous materials: synthesis and applications, Chem. Rev. 121 (2021) 12278–12326.

[19] L. Li, X.S. Wang, T.F. Liu, J.H. Ye, Titanium-based MOF materials: from crystal engineering to photocatalysis, Small Methods 4 (2020) 2000486.

[20] H.L. Nguyen, T.T. Vu, D. Le, T.L.H. Doan, V.Q. Nguyen, N.T.S. Phan, A titanium-organic framework: engineering of the band-gap energy for photocatalytic property enhancement, ACS Catal. 7 (2017) 338–342.

[21] H. Huang, X.S. Wang, D. Philo, F. Ichihara, H. Song, Y.X. Li, D. Li, T. Qiu, S. Y. Wang, J.H. Ye, Toward visible-light-assisted photocatalytic nitrogen fixation: a titanium metal organic framework with functionalized ligands, Appl. Catal. B 267 (2020) 118686.

[22] Z. Li, J.D. Xiao, H.L. Jiang, Encapsulating a Co(II) molecular photocatalyst in metal-organic framework for visible-light-driven H_2 production: boosting catalytic efficiency via spatial charge separation, ACS Catal. 6 (2016) 5359–5365.

[23] T.Q. Zhou, S.Z. Wang, C.J. Zhang, Y. Yao, Y.Y. Chen, S.X. Lu, X.Y. Liao, Preparation of Ti-MOFs for efficient adsorptive desulfurization: synthesis, characterization, and adsorption mechanisms, Fuel 339 (2023) 127396.

[24] P. Qiu, Y. Yao, S.X. Lu, L.G. Chen, Y.Y. Chen, X.Y. Liao, Decorating Ti-MOF with noble metal as highly efficient photocatalyst: fine-tuning the valence band to co-production of 2,5-diformylfuran and H_2, Fuel 351 (2023) 129043.

[25] Z.X. Sun, K. Sun, M.L. Gao, O. Metin, H.L. Jiang, Optimizing Pt electronic states through formation of a schottky junction on non-reducible metal-organic frameworks for enhanced photocatalysis, Angew. Chem. Int. Ed. 61 (2022) e202206108.

[26] Y. Wang, W. Zhang, D. Li, J.P. Guo, Y. Yu, K.J. Ding, W.B. Duan, X.Y. Li, H.Y. Liu, P.K. Su, B. Liu, J.F. Li, Efficient schottky junction construction in metal-organic frameworks for boosting H_2 production activity, Adv. Sci. 8 (2021) 2004456.

[27] H.M. Wang, R. Zhao, J.Q. Qin, H.X. Hu, X.W. Fan, X. Cao, D. Wang, MIL-100(Fe)/ Ti_3C_2 MXene as a schottky catalyst with enhanced photocatalytic oxidation for nitrogen fixation activities, ACS Appl. Mater. Interfaces 11 (2019) 44249–44262.

[28] Z.G. Tai, G.T. Sun, T. Wang, Z.H. Li, J.G. Tai, Construction of PdS@MIL-125-NH$_2$@ ZnS type-II heterostructure with efficient charge separation for boosted photocatalytic hydrogen evolution, J. Mater. Sci. Technol. 145 (2023) 116–124.

[29] J. Jin, J.P. Kim, S.P. Wan, K.H. Kim, Y. Choi, P. Li, J. Kang, Z.Y. Ma, J.H. Lee, O. Kwon, D.W. Kim, J.H. Park, Hierarchical pore enhanced adsorption and photocatalytic performance of graphene oxide/Ti-based metal-organic framework hybrid for toluene removal, Appl. Catal. B 317 (2022) 121751.

[30] Y. Xiong, B. Li, Y.M. Gu, T. Yan, Z.G. Ni, S.H. Li, J.L. Zuo, J. Ma, Z. Jin, Photocatalytic nitrogen fixation under an ambient atmosphere using a porous coordination polymer with bridging dinitrogen anions, Nat. Chem. 15 (2022) 286–293.

[31] Y.C. Wei, W.Y. Zha, L.L. Wang, X.F. Ma, S.H. Zhang, R.J. Sa, H.X. Lin, Z.X. Ding, J. L. Long, X.Z. Fu, R.S. Yuan, In-situ formed surface complexes promoting NIR-light-driven carbonylation of diamine with CO on ultrathin $Co_2CO_3(OH)_2$ nanosheets, Appl. Catal. B 306 (2022) 121103.

[32] M.Y. Zhang, J.K. Li, R. Wang, S.N. Zhao, S.Q. Zang, T.C.W. Mak, Construction of core–shell MOF@COF hybrids with controllable morphology adjustment of COF shell as a novel platform for photocatalytic cascade reactions, Adv. Sci. 8 (2021) 2101884.

[33] R.X. Qin, K.L. Liu, Q.Y. Wu, N.F. Zheng, Surface coordination chemistry of atomically dispersed metal catalysts, Chem. Rev. 120 (2020) 11810–11899.

[34] P.L. Cheung, S.C. Kapper, T. Zeng, M.E. Thompson, C.P. Kubiak, Improving photocatalysis for the reduction of CO_2 through non-covalent supramolecular assembly, J. Am. Chem. Soc. 141 (2019) 14961–14965.

[35] J. Hu, Z.F. Huang, R.Y. Wang, X.W. Xu, Z.Y. Wang, H. Tang, L.L. Wang, Q.Q. Liu, Boosted charge transfer via coordinate bond construction in porphyrin metal–organic framework/$ZnIn_2S_4$ core–shell heterostructures, Inorg. Chem. 62 (2023) 6794–6807.

[36] G. Kladnik, M. Puppin, M. Coreno, M. de Simone, L. Floreano, A. Verdini, A. Morgante, D. Cvetko, A. Cossaro, Ultrafast charge transfer pathways through a prototype amino-carboxylic molecular junction, Nano Lett. 16 (2016) 1955–1959.

[37] Y.P. Wu, W. Zhou, J. Zhao, W.W. Dong, Y.Q. Lan, D.S. Li, C. Sun, X. Bu, Surfactant-assisted phase-selective synthesis of new cobalt MOFs and their efficient electrocatalytic hydrogen evolution reaction, Angew. Chem. Int. Ed. 56 (2017) 13001–13005.

[38] J. Zhao, X. Liu, Y.P. Wu, D.S. Li, Q.C. Zhang, Surfactants as promising media in the field of metal-organic frameworks, Coord. Chem. Rev. 391 (2019) 30–43.

[39] M. Xu, D. Li, K. Sun, L. Jiao, C. Xie, C. Ding, H.L. Jiang, Interfacial microenvironment modulation boosting electron transfer between metal nanoparticles and MOFs for enhanced photocatalysis, Angew. Chem. Int. Ed. 60 (2021) 16372–16376.

[40] L.T. Shi, C.C. Wu, Y. Wang, Y.H. Dou, D. Yuan, H. Li, H.W. Huang, Y. Zhang, I. D. Gates, X.D. Sun, T.Y. Ma, Rational design of coordination bond connected metal organic frameworks/MXene hybrids for efficient solar water splitting, Adv. Funct. Mater. 32 (2022) 2202571.

[41] J.X. Liu, F.F. Li, J.R. Lu, R. Li, Y.F. Wang, Y.W. Wang, X.C. Zhang, C.M. Fan, R. P. Zhang, Atomically dispersed Palladium-Ethylene Glycol- Bismuth oxybromide for photocatalytic nitrogen fixation: insight of molecular bridge mechanism, J. Colloid Interf. Sci. 603 (2021) 17–24.

[42] X.Q. Xie, N. Zhang, Positioning MXenes in the photocatalysis landscape: competitiveness, challenges, and future perspectives, Adv. Funct. Mater. 30 (2020) 2002528.

[43] Y.P. Liu, Y.H. Li, X.Y. Li, Q. Zhang, H. Yu, X.W. Peng, F. Peng, Regulating electron–hole separation to promote photocatalytic H_2 evolution activity of nanoconfined Ru/MXene/TiO_2 catalysts, ACS Nano 14 (2020) 14181–14189.

[44] M.D. Cai, X.Q. Zha, Z.Z. Zhuo, J.Q. Bai, Q. Wang, Q. Cheng, Y.X. Wei, S. Sun, Enhanced photocatalytic hydrogen production of $ZnIn_2S_4$ by using surface-engineered $Ti_3C_2T_x$ MXene as a cocatalyst, Materials 16 (2023) 2168.

[45] M.H. Ye, X. Wang, E.Z. Liu, J.H. Ye, D.F. Wang, Boosting the photocatalytic activity of P25 for carbon dioxide reduction by using a surface-alkalinized titanium carbide MXene as cocatalyst, ChemSusChem 11 (2018) 1606–1611.

[46] A. Sarycheva, Y. Gogotsi, Raman spectroscopy analysis of the structure and surface chemistry of $Ti_3C_2T_x$ MXene, Chem. Mater. 32 (2020) 3480–3488.

[47] Q. Xi, F.X. Xie, J.X. Liu, X.C. Zhang, J.C. Wang, Y.W. Wang, Y.F. Wang, H.F. Li, Z. B. Yu, Z.J. Sun, X. Jian, X.M. Gao, J. Ren, C.M. Fan, R. Li, In situ formation $ZnIn_2S_4$/Mo_2TiC_2 schottky junction for accelerating photocatalytic hydrogen evolution kinetics: manipulation of local coordination and electronic structure, Small 19 (2023) 2300717.

[48] P.V. Hlophe, L.C. Mahlalela, L.N. Dlamini, A composite of platelet-like orientated $BiVO_4$ fused with MIL-125(Ti): synthesis and characterization, Sci. Rep. 9 (2019) 10044.

[49] C. Petit, T.J. Bandosz, Synthesis, characterization, and ammonia adsorption properties of mesoporous metal-organic framework (MIL(Fe))-graphite oxide composites: exploring the limits of materials fabrication, Adv. Funct. Mater. 21 (2011) 2108–2117.

[50] X.Z. Yuan, H. Wang, Y. Wu, G.M. Zeng, X.H. Chen, L.J. Leng, Z.B. Wu, H. Li, One-pot self-assembly and photoreduction synthesis of silver nanoparticle-decorated reduced graphene oxide/MIL-125(Ti) photocatalyst with improved visible light photocatalytic activity, Appl. Organomet. Chem. 30 (2016) 289–296.

[51] Z.F. Zhao, D. Yang, H.J. Ren, K. An, Y. Chen, Z.Y. Zhou, W.J. Wang, Z.Y. Jiang, Nitrogenase-inspired mixed-valence MIL-53(FeII/FeIII) for photocatalytic nitrogen fixation, Chem. Eng. J. 400 (2020) 125929.

[52] C.T. Saouma, S. Richard, S. Smolders, M.F. Delley, R. Ameloot, F. Vermoortele, D. E. De Vos, J.M. Mayer, Bulk-to-surface proton-coupled electron transfer reactivity of the metal-organic framework MIL-125, J. Am. Chem. Soc. 140 (2018) 16184–16189.

[53] Y. Li Ping, X. Jia Cheng, Y. Dan Hua, L. Lin, X. Yun Peng, L. Zhong Min, Synthesis of high-crystallinity MIL-125 with outstanding xylene isomer separation performance, Chin. J. Catal. 42 (2021) 2313–2321.

[54] C.H. Hendon, D. Tiana, M. Fontecave, C. Sanchez, L. D'arras, C. Sassoye, L. Rozes, C. Mellot-Draznieks, A. Walsh, Engineering the optical response of the titanium-MIL-125 metal–organic framework through ligand functionalization, J. Am. Chem. Soc. 135 (2013) 10942–10945.

[55] Z.F. Zhao, H.J. Ren, D. Yang, Y. Han, J.F. Shi, K. An, Y. Chen, Y.H. Shi, W.H. Wang, J.D. Tan, X. Xin, Y. Zhang, Z.Y. Jiang, Boosting nitrogen activation via bimetallic organic frameworks for photocatalytic ammonia synthesis, ACS Catal. 11 (2021) 9986–9995.

[56] X.J. Chen, J. Wang, Y.Q. Chai, Z.J. Zhang, Y.F. Zhu, Efficient photocatalytic overall water splitting induced by the giant internal electric field of a g-C_3N_4/rGO/PDIP Z-scheme heterojunction, Adv. Mater. 33 (2021) e2007479.

[57] G. Liu, J. Shi, F. Zhang, Z. Chen, J. Han, C. Ding, S. Chen, Z. Wang, H. Han, C. Li, A tantalum nitride photoanode modified with a hole-storage layer for highly stable solar water splitting, Angew. Chem. Int. Ed. 53 (2014) 7295–7299.

[58] Y.Z. Zhang, X. Chen, S.Y. Zhang, L.F. Yin, Y. Yang, Defective titanium dioxide nanobamboo arrays architecture for photocatalytic nitrogen fixation up to 780 nm, Chem. Eng. J. 401 (2020) 126033.

[59] H.Y. Wu, X. Li, Y. Cheng, Y.H. Xiao, R.F. Li, Q.P. Wu, H. Lin, J. Xu, G.Q. Wang, C. Lin, X.Y. Chen, Y.S. Wang, Plasmon-driven N_2 photofixation in pure water over MoO_{3-x} nanosheets under visible to NIR excitation, J. Mater. Chem. A 8 (2020) 2827–2835.

[60] G.Q. Zhang, X. Yang, C.X. He, P.X. Zhang, H.W. Mi, Constructing a tunable defect structure in TiO_2 for photocatalytic nitrogen fixation, J. Mater. Chem. A 8 (2020) 334–341.

[61] J. Di, J.X. Xia, M.F. Chisholm, J. Zhong, C. Chen, X.Z. Cao, F. Dong, Z. Chi, H. L. Chen, Y.X. Weng, J. Xiong, S.Z. Yang, H.M. Li, Z. Liu, S. Dai, Defect-tailoring mediated electron-hole separation in single-unit-cell Bi_3O_4Br nanosheets for boosting photocatalytic hydrogen evolution and nitrogen fixation, Adv. Mater. 31 (2019) 1807576.

[62] S.Y. Wang, X. Hai, X. Ding, K. Chang, Y.G. Xiang, X.G. Meng, Z.X. Yang, H. Chen, J. H. Ye, Light-switchable oxygen vacancies in ultrafine Bi_5O_7Br nanotubes for boosting solar-driven nitrogen fixation in pure water, Adv. Mater. 29 (2017) 1701774.

[63] C.L. Mao, L.H. Yu, J. Li, J.C. Zhao, L.Z. Zhang, Energy-confined solar thermal ammonia synthesis with K/Ru/$TiO_{2-x}H_x$, Appl. Catal. B 224 (2018) 612–620.

[64] C.M. Zhang, Y.L. Xu, C.D. Lv, L.C. Bai, J. Liao, Y.C. Zhai, H.W. Zhang, G. Chen, Amorphous engineered cerium oxides photocatalyst for efficient nitrogen fixation, Appl. Catal. B 264 (2020) 118416.

[65] D.X. Jiao, Y.J. Liu, Q.H. Cai, J.X. Zhao, Coordination tunes the activity and selectivity of the nitrogen reduction reaction on single-atom iron catalysts: a computational study, J. Mater. Chem. A 9 (2021) 1240–1251.

[66] X.N. Zheng, Y. Liu, Y. Yao, Trimetallic single-cluster catalysts for electrochemical nitrogen reduction reaction: activity prediction, mechanism, and electronic descriptor, Chem. Eng. J. 426 (2021) 130745.

[67] G.K. Zheng, L. Li, Z.Q. Tian, X.W. Zhang, L. Chen, Heterogeneous single-cluster catalysts (Mn3, Fe3, Co3, and Mo3) supported on nitrogen-doped graphene for robust electrochemical nitrogen reduction, J. Energy Chem. 54 (2021) 612–619.